

RESEARCH ARTICLE

Wavelet scattering- and object detection-based computer vision for identifying dengue from peripheral blood microscopy

Liora Rosvin Dsilva¹ | Shivani Harish Tantri¹ | Niranjana Sampathila¹  |
Hilda Mayrose¹ | G. Muralidhar Bairy¹ | Sushma Belurkar² |
Kavitha Saravu³ | Krishnaraj Chadaga⁴ | Abdul Hafeez-Baig⁵

¹Department of Biomedical Engineering, Manipal Institute of Technology, Manipal Academy of Higher Education (MAHE), Manipal, India

²Department of Pathology, Kasturba Medical College, Manipal Academy of Higher Education (MAHE), Manipal, India

³Department of Infectious Diseases, Kasturba Medical College, Manipal Academy of Higher Education (MAHE), Manipal, India

⁴Department of Computer Science and Engineering, Manipal Institute of Technology, Manipal Academy of Higher Education (MAHE), Manipal, India

⁵Faculty of Business, Education, Law and Arts, University of Southern Queensland, Toowoomba, Queensland, Australia

Correspondence

Niranjana Sampathila and Hilda Mayrose, Department of Biomedical Engineering, Manipal Institute of Technology, Manipal Academy of Higher Education (MAHE), Manipal, India.

Email: niranjana.s@manipal.edu; hilda.mayrose@manipal.edu

Abstract

Dengue fever infection is a global health concern. Early disease detection is crucial for averting complications and fatality. Characteristic morphological changes in lymphocytes can be observed on a peripheral blood smear (PBS) in cases of dengue infection. In this research, we have developed automated computer vision models for dengue detection on PBS images using two approaches: wavelet scattering transform (WST)-based feature engineering and classification and You Only Look Once (YOLO)-based deep transfer learning for object detection. In the former, Morlet wavelet scattering features extracted from lymphocytes were used as input for five shallow classifiers for image classification. Among these, the support vector machine achieved the best results of 98.7% accuracy using 10-fold cross-validation. In the latter, computer vision-enabled object detection was implemented using five YOLOv8 scaled variants. Among these, YOLOv8s and YOLOv8l attained identical best mean accuracy of $99.3\% \pm 1.4\%$ across five independent experiments. Our results confirmed the feasibility and excellent diagnostic accuracy for both WST- and YOLOv8-enabled computer vision approaches for diagnosing dengue infection in PBS images. This research incorporates deep machine learning along with AI technology to enhance understanding and capabilities in automated Dengue diagnosis. The significance of this research extends to the broader domain of mosquito-borne illnesses. However, it is important to note that the findings are limited to the dataset used by the researchers.

KEYWORDS

computer vision, dengue, lymphocytes, WST, YOLOv8

This is an open access article under the terms of the [Creative Commons Attribution](https://creativecommons.org/licenses/by/4.0/) License, which permits use, distribution and reproduction in any medium, provided the original work is properly cited.

© 2024 The Authors. *International Journal of Imaging Systems and Technology* published by Wiley Periodicals LLC.

1 | INTRODUCTION

Mosquito-borne illnesses caused by arboviruses are important global public health concerns.^{1–3} In developing countries, one of the most significant viral infections spread by mosquitoes is dengue.⁴ Dengue is transmitted to humans through the bites of infected female *Aedes aegypti* mosquitoes. It has a high incidence of infection, which has led to widespread epidemics and public health crises.⁵ It has been reported that there are 390 million dengue virus infections annually, of which 96 million manifest clinically.⁶ An estimated 3.9 billion people worldwide are at risk of contracting the dengue virus infection,⁶ and the disease is endemic in more than 100 countries, with Asia accounting for over 70% of the global disease burden.⁶

Dengue is a complex disease caused by distinct dengue virus serotypes that present with a broad spectrum of clinical manifestations, ranging from mild debilitating febrile illness like dengue fever to life-threatening dengue hemorrhagic fever and dengue shock syndrome.⁷ These three conditions likely represent progressively severe stages of a continuous dengue disease spectrum.^{7,8} It has been estimated that 50–100 million cases of dengue fever, 500 000 cases of dengue hemorrhagic fever/dengue shock syndrome, and more than 20 000 dengue-related deaths occur annually.⁶ Most primary infections are caused by a single dengue virus serotype, which leads to an enervating but nonfatal illness. Symptoms start 4–10 days after infection and persist for 2–7 days. High temperature (40°C or more), severe headache, eye pain, joint pain, nausea, vomiting, swollen glands, and rash are typical symptoms.⁶ While there is no definitive treatment against the dengue virus, early and accurate diagnosis of dengue fever is crucial for instituting heightened surveillance and timeous supportive measures in the event of progression to severe dengue. Routine laboratory tests like complete blood count and coagulation tests are commonly used to detect and monitor for dengue-associated complications of thrombocytopenia and coagulopathy⁸ but are non-specific. Similarly, abnormal results of serological tests like hemagglutination inhibition and plaque reduction neutralization can provide some support to corroborate dengue infection but are not diagnostic.⁹ For a definitive diagnosis of dengue infection, advanced laboratory-based techniques are required to detect the dengue virus, its viral ribonucleic acid, viral antigens, or anti-dengue antibodies in the patient's blood.¹⁰ Reverse transcriptase polymerase chain reaction¹⁰ is considered the gold standard for confirming the presence of viral ribonucleic acid in infected sera.⁸ Other confirmatory tests use enzyme-linked immunosorbent assay methods to either detect viral antigens like the non-structural

protein, NS1, or viral immunoglobulin M and G antibodies in sera. Both these techniques require sophisticated equipment and skilled expertise,^{9,11} are expensive, and cannot be readily deployed for high-volume real-time detection.

Digitization of whole-slide pathological images has facilitated the use of artificial intelligence-enabled tools for medical diagnosis.^{12–14} In particular, computer vision-based approaches have been harnessed for object detection, segmentation, and classification tasks involving digitized medical images.^{12,15} Both machine learning and deep learning approaches can be deployed in automated digital pathology-based computer vision applications.^{16–18} Machine learning algorithms are trained using discriminative features extracted from image datasets; once trained, the algorithms can generalize and make predictions on unseen new data. A subset of machine learning, deep learning, uses convolutional neural networks (CNNs) to construct higher-level representations of image data to make their predictions.¹⁹ Due to the burgeoning interest in and accelerated development of neural networks, deep learning-based computer vision applications in medical image classification, localization, and object detection have garnered significant clinical traction for disease diagnosis and prognostication.^{20,21} In repetitive and time-intensive tasks like manual interpretation of medical images, computer vision can potentially perform the diagnostic classification automatically with higher accuracy and reproducibility than human readers, thereby reducing the time burden on laboratory staff.^{22,23} Moreover, in disease outbreaks affecting large populations, human analysis may become overwhelmed by the high volume of samples that need to be processed and analyzed. In such scenarios, computer vision methods can perform high-throughput analysis efficiently, effectively freeing up time for healthcare workers to attend to the important downstream treatment of appropriately diagnosed patients.^{23,24}

1.1 | Background

The peripheral blood smear (PBS) is a method of manually staining a glass slide with a small amount of blood to depict and preserve the morphological characteristics of various blood components, including red blood cells, white blood cells (which comprise neutrophils and lymphocytes), and platelets. A digital microscope can be used to photograph the PBS to obtain digitized PBS images for offline expert interpretation, archival, as well as, increasingly, artificial intelligence-enabled analysis of differential morphological characteristics of blood cells in health and in disease.²⁵ In viral infections, lymphocyte counts

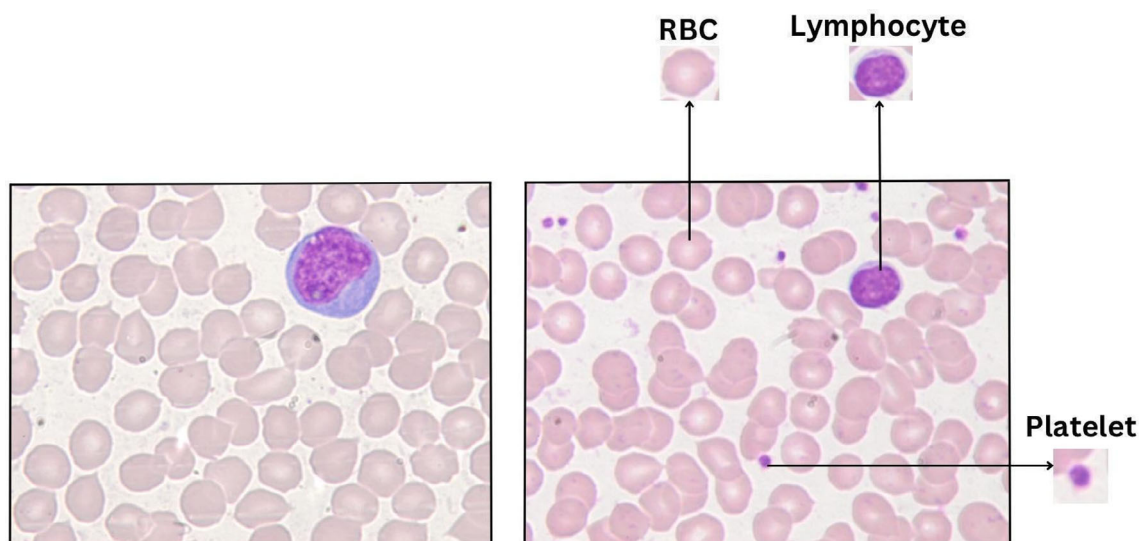


FIGURE 1 Leishman stained 100 \times peripheral blood smear images of dengue-infected patients (left) and healthy subjects (right). In the former, the lymphocyte appears larger with a bigger, irregular nucleus and abundant cytoplasm.

are often elevated, and the cell may undergo morphological changes. In dengue infection, abnormal lymphocytes called atypical plasmacytoid lymphocytes are seen in the blood, induced by an immune reaction to the dengue virus.^{26,27} The atypical lymphocytes exhibit changes in the size of the nucleus and cytoplasm, color, and shape²⁵: the nucleus becomes bigger and irregular; the cytoplasm is more abundant and bluer²⁷ (Figure 1). These altered feature parameters can be exploited for developing tests to detect the presence of dengue-infected blood cells.²⁵

1.2 | Literature review

We were motivated to develop automated computer vision diagnostic models for dengue diagnosis based on the morphological features of lymphocytes on the PBS. Several researchers have capitalized on disease-associated altered blood cell morphology to develop PBS-based machine-learning models for the detection of diseases. Deb et al.²⁸ studied geometric features like aspect ratio and Fourier descriptors of normal and anemic red blood cells and incorporated them into their model for detecting anemia. Bashar et al.²⁹ developed a support vector machine (SVM)-based model that classified various stages of malaria parasites on PBS images using textural feature descriptors like the histogram of oriented gradients, gray-level co-occurrence matrix, and local binary pattern, as well as color feature descriptors like StatMom, and color histogram. Moshavash et al.³⁰ used a gray-level co-occurrence matrix and local binary pattern to extract textural features from white blood cells to detect acute lymphoblastic leukemia cells automatically. Nikitaev et al.³¹

applied wavelet transform to the nuclei of white blood cells to extract discriminative features for automated diagnosis of acute leukemia. In their dengue diagnostic model, Mayrose et al.³² first segmented lymphocyte nuclei on PBS images using Otsu's global thresholding method, and then applied local binary pattern and pre-trained MobileNetV2 to extract discriminative textural and deep features, respectively, from the lymphocyte nuclei. Informative features were selected using the ReliefF (Relief Feature) algorithm and then fed to a SVM classifier. Their model attained excellent accuracy, sensitivity, and specificity of 95.74%, 98.14%, and 92.50%, respectively. Nawa et al.³³ studied dengue-infected white blood cells on PBS that had been specially stained with immunochemical streptavidin-biotin peroxidase complex coloring. Image contrast was enhanced by Gram-Schmidt orthogonalization, which facilitated the segmentation of white blood cell images using Otsu's thresholding technique. The image histograms were used as features, which were input to SVM for classification. The proposed model attained fair 83.94% accuracy, 81.61% precision, 92.21% sensitivity, and 73.33% specificity for dengue detection.

For developing our dengue detection model, we were particularly interested in the wavelet scattering transform, and You Only Look Once (YOLO) algorithms, which exemplified handcrafted multilevel feature engineering and pre-trained deep transfer learning approaches, respectively. WST is a wavelet transform-based method that extracts features in both time and frequency domains.^{34,35} Compared with standard wavelet transforms, wavelet image scattering constructs low-variance image representations that are insensitive to time and frequency deformations.^{36–38} An advantage of WST over CNN-based

methods is its use of fixed and preset wavelet filters, which obviates the need for high-volume data samples to train filter responses. Hence, WST is preferred for limited training datasets.³⁸ There is a paucity of studies on the use of WST-based feature extraction in dengue diagnostic models. In their glaucoma diagnostic model, Agboola et al.³⁹ stage-wise decomposed retinal fundus images by inputting them into a wavelet scattering network constructed in MATLAB. They adopted a feature learning algorithm called invariant scattering convolution network, which facilitated the automatic learning of features. The model attained F1 scores of 98% and 85% with SVM and logistic regression, respectively, using random data splitting; and F1 scores of 89% and 83% with SVM and logistic regression, respectively, using hospital-based splitting.

Razali et al.⁴⁰ proposed a model for classifying benign versus malignant breast masses and fatty versus fibro glandular tissue on digital mammograms that employed both handcrafted feature engineering and deep learning approaches to train a relatively modest dataset of 112 mammogram images. The latter were input to gray-level co-occurrence matrix and WST as well as CNN to generate features. Different feature fusion combinations of these were input to an ensemble k-nearest neighbors (kNN) classifier. On 10-fold cross-validation (CV), their model attained 98.0% and 99.3% accuracies for mass and tissue classification, respectively. The authors concluded that wavelet representation enhanced feature descriptors for spatial-frequency analysis, which mitigated CNN overfitting on their limited dataset, and contributed to their excellent results.

YOLO algorithms have gained popularity for diverse computer vision tasks like object identification, segmentation, pose estimation, tracking, and classification, owing to their high detection accuracy and processing speed.⁴¹ Rocha et al.⁴² combined various YOLO versions—YOLOv3, YOLOv4, Scaled-YOLOv4, and YOLOv5—with single shot multibox detector, EfficientNet, and faster region-based CNN models for detection of malaria parasites in PBS images. On a 3065-image study dataset composed of four public datasets, which encompassed labels of healthy and infected blood cells, four species of malaria parasites, four stages of the *Plasmodium vivax* life cycle, and four stages of the infected cells' life cycle, their model attained mean average precisions of 41.15%, 35.01%, 35.9%, and 63.30% for single shot multibox detector, EfficientNet, faster region-based CNN, and YOLOv5, respectively. In their cervical cancer cell detection model, Jia et al.⁴³ improved upon the YOLOv3 model by substituting the ResNet layer in the branch prediction with a dense block, coupled with the S3pool algorithm. The model attained a significant 50% reduction in optimized network loss function value, a 3.03% increase in mean

average precision, and an improved 78.87% average detection accuracy, which surpassed single shot multibox detector, YOLOv3, and ResNet50 by 8.02%, 8.22%, and 4.83% respectively. Khandekar et al.⁴⁴ developed a YOLOv4-based object detection algorithm for detecting blast cells on PBS images. These are abnormal white blood cells associated with acute lymphoblastic leukemia. A total of 108 and 10 661 images from two public datasets were pre-processed and augmented before being used to train the YOLOv4 network. On the smaller dataset, the model attained overall mean average precision, recall, and F1 score of 95.57%, 0.92%, and 0.92%, respectively, and on the larger dataset, 98.57%, 0.96%, and 0.92%, respectively.

In this unique research, researchers aimed to implement WST-based feature extraction and YOLOv8-enabled object detection in parallel to characterize lymphocytes in PBS images for the automated binary classification of dengue infection versus normal. To our knowledge, there has been no prior publication on the use of either of these techniques for dengue detection from PBS images. This work makes several significant contributions: (i) it utilizes a unique dataset that is not publicly available; (ii) it applies WST-based features for dengue detection; (iii) it employs the latest version of YOLO, known as YOLOv8, to automate the process of dengue detection. These contributions collectively enhance our understanding and capabilities in automated dengue diagnosis based on lymphocyte characteristics.

2 | METHODOLOGY

2.1 | Study dataset

The dataset comprised two classes of 163 “Dengue” and 151 “Normal” images digitized from peripheral blood smears (PBSs) obtained from 29 and 30 patients with and without active dengue infection, respectively. After approval by the hospital ethics committee, study participants were identified from hospital discharge ICD codes at Kasturba Hospital, Manipal, and PBSs retrieved from the on-site hematology laboratory. The Leishman-stained PBSs had been manually prepared on glass slides; from each of these, a number of PBS images at various regions of interest were acquired by oil immersion field photography—a drop of liquid paraffin oil was spread onto the glass slide prior to image capture—using an Olympus DP25 digital microscope with 100× magnification and 2560 × 1920 resolution. Specifically, the regions of interest were focused on an area between the head and tail of the PBS: unlike the body, which contained a large number of red blood cells, this area had fewer red blood

cells spread out more evenly, which offered better visualization of lymphocytes, the cells of interest.

2.2 | Machine learning with wavelet scattering features

2.2.1 | Wavelet scattering transform

In this handcrafted machine learning approach, we combined WST with downstream shallow classifiers. In our model, we used Morlet wavelets, which are anisotropic, sensitive to rotations and directions, and effective for tracking feature-oriented segment and edge image information.³⁹ As a proof-of-concept, wavelet scattering networks based on Morlet wavelets-extracted features have been proposed in computationally lightweight algorithms for classifying images of numerical digits⁴⁵ and gray-scale textures.⁴⁶ The WST function comprises three successive stages: convolution, nonlinearity transform, and convolution averaging using complex wavelets, modulus operation, and scale function, respectively. Dilated mother wavelets with different scaling levels can be used as wavelet functions in the scattering transform. In our model, we used the Morlet wavelet as the mother wavelet. The data were first convolved with the scaling function to yield the zeroth-order scattering coefficients.^{47,48}

$$S[0] = i * \varphi \quad (1)$$

where i represents input data; φ , scaling function, and $S[0]$, zeroth-order scattering coefficients. The input data were then subjected to wavelet transform using each wavelet filter in the first filter bank, and the modulus of each filtered output was calculated. These moduli were averaged with the scaling filter to yield the first-order scattering coefficients.^{47,48}

$$S[1] = |i * \psi_{j1}| * \varphi \quad (2)$$

where $\{\psi_{j,k}\}$ represents the wavelet, and $S[1]$, first-order scattering coefficient. The wavelet filters encompassed different scales and rotations with respect to the image, which enabled a comprehensive analysis of the input data. By iterating the above steps, the second-order scattering coefficients were computed.^{47,48}

$$S[2] = \left\| |i * \psi_{j1}| * \psi_{j2}| * \varphi \right\| \quad (3)$$

where $S[2]$ represents second-order scattering coefficients, they were then used to decompose the PBS image (Figure 2).

2.2.2 | Implementing the wavelet scattering network

The experiment was performed on a core i7 processor and 64 GB RAM. WST was implemented in the MATLAB programming environment using the Image Processing Toolbox and Wavelet Toolbox. Complex-valued two-dimensional Morlet filter banks were configured, corresponding to the two scattering stages. The outcome of wavelet image scattering was influenced by various framework parameters: invariance scale, quality factor, and number of rotations. The invariance scale determines the spatial extent of the scaling filter in both the row and column dimensions. The default setting is half the smaller image dimension, which, in our case, was set to 960 ($=0.5 \times 1920$). The quality factor is the number of wavelet filters per octave in each filter bank. Minimizing the quality factor is preferred since increasing it does not enhance the discriminative ability of the feature space.⁴⁹ In our model, one wavelet filter per octave was set in each filter bank to minimize the computational workload. Each wavelet in each filter bank has an equally spaced angle between 0 and π radians, and is rotated clockwise for a varying number of rotations. In our experiments, invariance scale and quality factor were fixed, while the number of rotations varied from 1 to 6 per wavelet in the first and second filter banks. The number of generated feature sets ranged from 37 to 1057. Following extraction, the wavelet scattering features were normalized to a range of 0–1 and then stored as matrices on Microsoft Excel: rows and columns of the spreadsheet represented individual PBS images and features, respectively.

2.2.3 | Classification algorithms

The researchers adopted five established classifiers commonly used in supervised learning were deployed: decision tree (DT), discriminant analysis, SVM, kNN, and multilayer perceptron (MLP). DT follows a top-down recursive approach based on the data class labels to build a tree-like structure, where leaves represent outcome labels and branches combinations of input features that led to the outcomes.^{50,51} The discriminant analysis relies on discriminant variables, which have been selected based on prior knowledge to represent unique characteristics expected to differ among the groups, to derive a set of equations from input features to assign labels to the samples.⁵² Linear discriminant analysis (LDA) was used in our model. SVM uses data from binary classes to construct a maximum margin hyperplane separating the two classes for data classification and regression analysis.⁵³ It

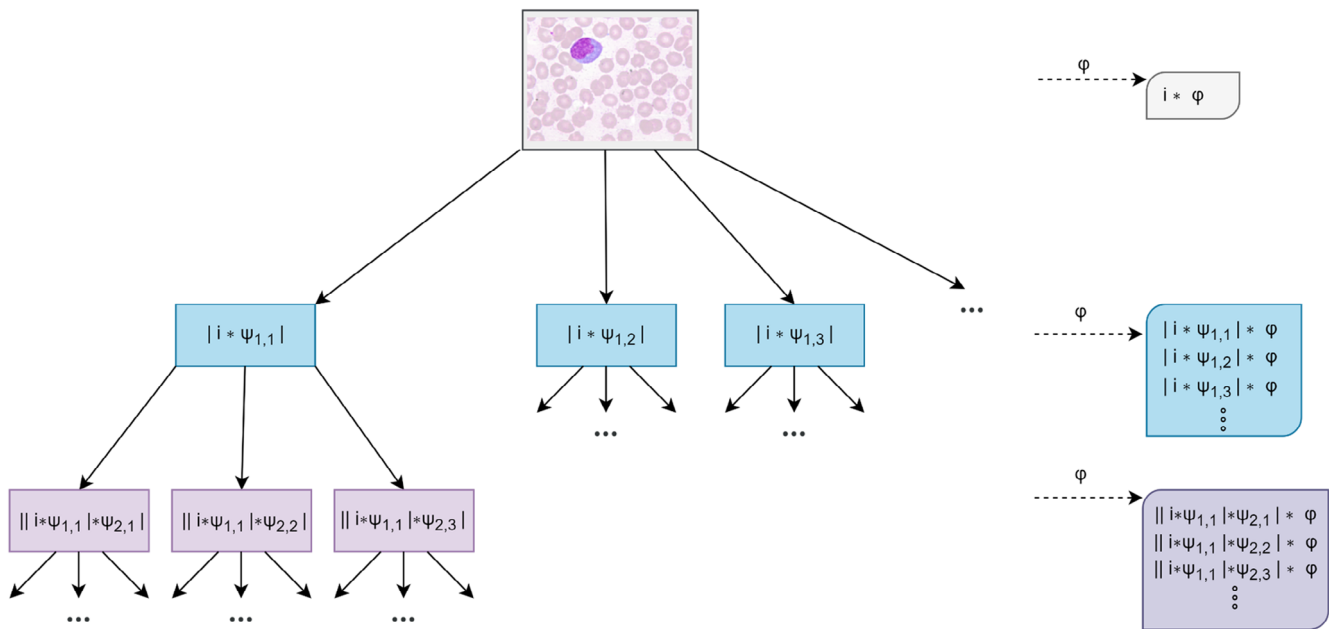


FIGURE 2 Decomposition of a peripheral blood smear image using second-order wavelet scattering transform.

TABLE 1 Parameter specifications of model classifiers.

Classifier	Model specifications
Decision tree	Preset: fine tree; maximum number of splits: 100; split criterion: Gini's diversity index; surrogate decision splits: off
Discriminant analysis	Preset: linear discriminant; covariance structure: full
Support vector machine	Preset: cubic support vector machine; kernel function: cubic; kernel scale: automatic; box constraint level: 1; multiclass method: one-vs.-one; standardize data: true
k-Nearest neighbors	Preset: fine k-nearest neighbors; number of neighbors: 1; distance metric: Euclidean; distance weight: equal; standardize data: true
Multilevel perceptron	Preset: medium neural network; number of fully connected layers: 1; first layer size: 25; activation: rectified linear unit; iteration limit: 1000; regularization strength (lambda): 0; standardized data: yes

works for datasets with separable and non-separable classes, the latter by using a kernel function to transform the data to a higher-dimensional space to facilitate linear hyperplane data separation.^{50,54} Cubic SVM, with the cubic kernel, was utilized in our model. By assigning an unknown instance to each class with reference to known instances, kNN assigns the class to a feature vector based on the majority class among its k nearest neighbors.⁵⁰ In our model, fine-grained kNN was employed, which

enabled precise differentiation between classes by considering the closest neighbor only, that is, with k set to 1. MLP, with input, hidden, and output layers, learns to distinguish between different classes through an initial learning phase: the neural network compares the predicted output with the correct output and adjusts its internal weights accordingly.⁵⁵ Its effectiveness is influenced by the structure, activation functions, and weight updating. The selected factors determine the number of input neurons, while the number of hidden neurons is based on the training data.^{56,57} In this work, medium MLP was used.

The above classifiers were applied to input matrixes, which embodied PBS image data with corresponding WST-based features, using MATLAB Classification Learner Toolbox (Table 1). We adopted a 10-fold CV strategy for our data, which would minimize model overfitting and, by averaging accuracies across all folds, maximize the generalizability of the results.

2.3 | Object detection with YOLOv8 architecture

2.3.1 | YOLOv8 architecture

We used YOLOv8, the latest version of the YOLO algorithm by Ultralytics, which is available in five scaled variants: YOLOv8n (nano), YOLOv8s (small), YOLOv8m (medium), YOLOv8l (large), and YOLOv8x (extra-large).⁴¹ These models differ in size and parameter count of their feature

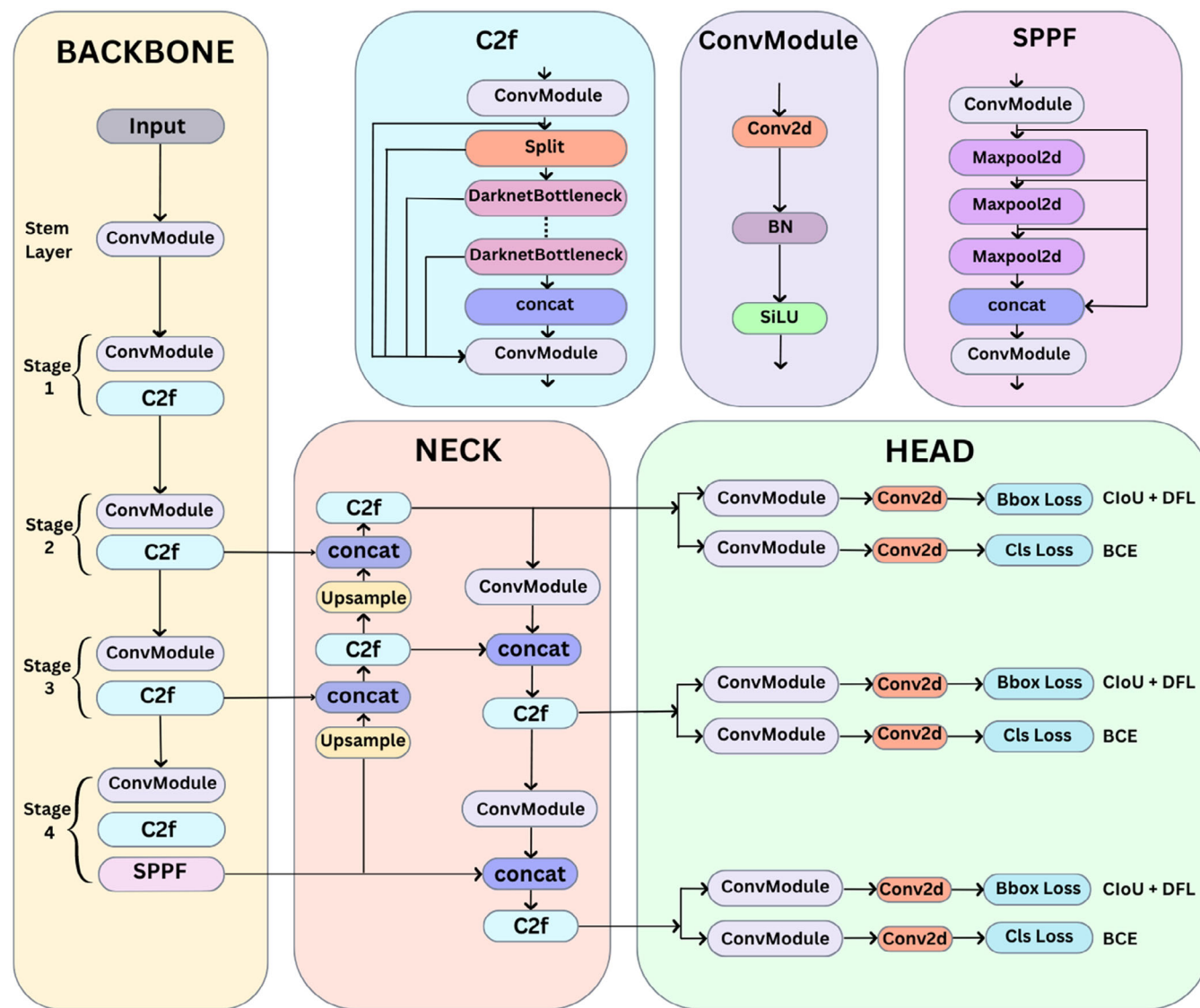


FIGURE 3 Block diagram of YOLOv8 (You Only Look Once version 8) model. Bbox loss, bounding box loss; BCE, binary cross entropy; BN, batch normalization; C2f, C2f module; CIoU, complete intersection over union; Cls loss, classification loss; concat, concatenation; Conv2d, two-dimensional convolution; ConvModule, convolution module; DFL, distribution focal loss; SiLU, sigmoid linear unit; SPPF, spatial pyramid pooling-fast.

extraction modules: YOLOv8x has the largest module size and parameter count, and YOLOv8n is the smallest. Similar to YOLOv5,⁵⁸ the YOLOv8 architecture consists of a backbone, neck, and head (Figure 3). The backbone extracts features from the input image using a series of convolutional layers and then splits the generated feature map into two parts using a cross-stage partial architecture: the first encompasses the output of the convolution operations; the second, the concatenated outputs of the current and previous portions. In so doing, the cross-stage partial architecture improves learning ability and reduces computational costs. Convolutional layers of the backbone include, among others, a C2f module and a spatial pyramid pooling-fast (SPPF) layer, which is an improved version of spatial

pyramid pooling. The C2f module integrates high-level features with contextual information, enhancing detection accuracy. The SPPF, the last layer of the backbone, processes features at various scales (along with subsequent convolution layers), which increases model inference speed.^{59,60} In the neck, upper layers acquire more information due to additional network layers, whereas lower layers preserve location information due to fewer convolution layers. In YOLOv8, the traditional YOLO neck architecture is replaced with a novel C2f module that incorporates feature pyramid network (FPN) and path aggregation network (PAN) architectures. FPN upsamples from top to bottom, and PAN downsamples from bottom to top, which increases the amount of feature information at the bottom

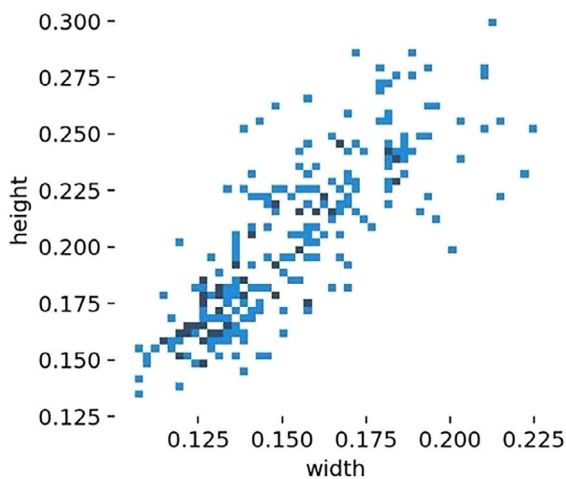


FIGURE 4 Scatter plot of the heights versus widths of bounding boxes. Every point corresponds to one of 251 manually annotated labels in the training dataset (130 and 121 in the “Dengue-infected” and “Normal” classes, respectively).

and top of the feature map, respectively. By merging the two feature outputs, which effectively integrated feature layer information across multiple scales and network layers, precise predictions were obtained for images of various sizes.⁶¹ The YOLOv8 head is designed to be decoupled: two distinct heads perform objectness, classification, and regression tasks separately in parallel. Each head processes feature maps generated by the backbone to infer the final model output of bounding boxes and object class probabilities. This enables each branch to concentrate on its specific duty, which improves model accuracy.⁶²

2.3.2 | Dataset pre-processing

Each image in the dataset was manually annotated using the Labelling Tool obtained from the GitHub repository. Bounding boxes were drawn around objects of interest, and image annotations were appended, which were saved in YOLO format as text files. The dataset comprised 314 PBS images; accordingly, the training dataset had 251 ($\approx 0.80 \times 314$) labels (Figure 4).

Following annotation, data augmentation was performed to introduce data variability, thereby creating a more diverse training dataset that would enhance the robustness and generalizability of the model. Various augmentation techniques^{63,64} were deployed, including (1) blurring input image using a random-sized kernel: maximum kernel size was set at the 3–7 range; and likelihood that transform would be used, at 0.01; (2) blurring input image using a median filter with random aperture linear size: maximum aperture linear size was set at the 3–7 range; and likelihood that transform would be used,

at 0.01; (3) applying contrast limited adaptive histogram equalization to input image: upper threshold value for contrast limiting was set at 4; grid size for histogram equalization, at (8, 8); and likelihood that transform would be used, at 0.01; and (4) converting input RGB image to gray-scale: likelihood that transform would be used was set at 0.01.

2.3.3 | Object detection model implementation

All five YOLOv8 models—YOLOv8n, YOLOv8s, YOLOv8m, YOLOv8l, and YOLOv8x—were trained from scratch on the study dataset, which was divided into training, validation, and testing sets at a split ratio of 80:10:10. Of note, the training process was expedited by transfer learning, which facilitated model creation with relatively modest datasets. The experiment was performed on a core i7 processor and 64 GB RAM. YOLOv8 models were implemented using Tesla K80 GPU on Google Colaboratory. Model-specific YAML data configuration files containing data parameters like a number of classes, class names, and data paths were built to serve as input for the YOLOv8 models. Stochastic gradient descent (SGD) and Adam optimizers were used during training. The training epoch number was set at 120, with eight images in each batch; the input image size, at the default resolution of 640; and SGD and Adam optimizer learning rates, at 0.001 and 0.0001, respectively. After completing model training, testing was conducted on previously unseen data.

3 | RESULTS

3.1 | Performance of machine learning with wavelet scattering features

At the various feature matrix sizes, which increased with the number of rotations (set at 1–6), all five classifiers yielded good classification accuracies exceeding 90% with a 10-fold CV (Table 2). Overall, the cubic SVM classifier attained the best accuracy of 98.7% for the 314×481 feature matrix (4 rotations), with negligible rates of misclassification (Figure 5) and excellent C-statistic of 0.9983 on receiver operating characteristic analysis.

3.2 | Performance of object detection using YOLOv8 algorithm

Performances of all five trained YOLOv8 variants were evaluated during initial training and validation. Results obtained on the validation dataset implied that training

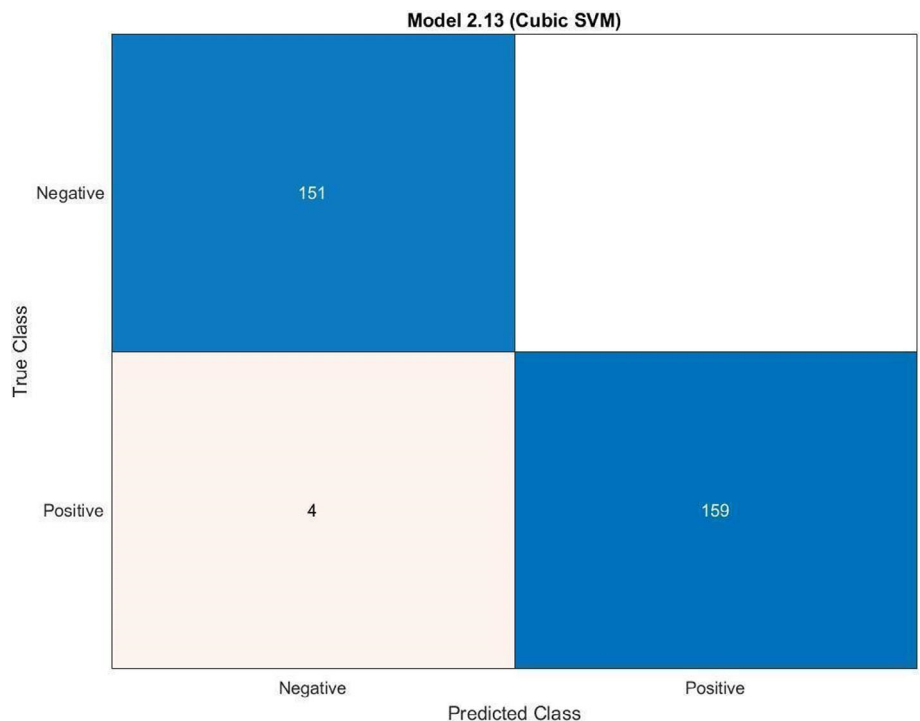
TABLE 2 Performance of machine learning with wavelet scattering features for dengue detection stratified by classifier and feature matrix size.

Number of rotations* (feature matrix)	Performance (%)				
	Fine DT	LDA	Cubic SVM	Fine kNN	Medium MLP
[1 1] (314 × 37)	Sen 89.57; Spe 93.37; F1 91.53; Acc 91.40	Sen 95.09; Spe 99.33; F1 97.17; Acc 97.10	Sen 95.09; Spe 98.67; F1 96.87; Acc 96.80	Sen 94.47; Spe 96.68; F1 95.64; Acc 95.50	Sen 98.15; Spe 97.35; F1 97.85; Acc 97.80
[2 2] (314 × 129)	Sen 93.25; Spe 92.71; F1 93.25; Acc 93.00	Sen 96.93; Spe 98.01; F1 97.52; Acc 97.50	Sen 96.31; Spe 98.67; F1 97.50; Acc 97.50	Sen 93.25; Spe 98.67; F1 95.89; Acc 95.90	Sen 96.93; Spe 97.35; F1 97.22; Acc 97.10
[3 3] (314 × 277)	Sen 93.25; Spe 96.02; F1 94.70; Acc 94.60	Sen 69.94; Spe 72.84; F1 71.68; Acc 71.30	Sen 96.93; Spe 99.33; F1 98.13; Acc 98.10	Sen 95.09; Spe 98.01; F1 96.57; Acc 96.50	Sen 98.15; Spe 96.02; F1 97.25; Acc 97.10
[4 4] (314 × 481)	Sen 92.64; Spe 95.36; F1 94.08; Acc 93.90	Sen 94.48; Spe 96.69; F1 95.65; Acc 95.50	Sen 97.55; Spe 100.00; F1 98.76; Acc 98.70	Sen 95.09; Spe 99.34; F1 97.18; Acc 97.10	Sen 97.55; Spe 96.69; F1 97.25; Acc 97.10
[5 5] (314 × 741)	Sen 89.57; Spe 91.39; F1 90.68; Acc 90.40	Sen 95.71; Spe 98.01; F1 96.89; Acc 96.80	Sen 96.32; Spe 99.34; F1 97.82; Acc 97.80	Sen 95.09; Spe 100.00; F1 97.48; Acc 97.50	Sen 98.16; Spe 97.35; F1 97.86; Acc 97.80
[6 6] (314 × 1957)	Sen 93.87; Spe 90.07; F1 92.45; Acc 92.00	Sen 95.09; Spe 99.34; F1 97.18; Acc 97.10	Sen 96.32; Spe 99.34; F1 97.82; Acc 97.80	Sen 93.87; Spe 100.00; F1 96.84; Acc 96.80	Sen 97.55; Spe 97.35; F1 97.55; Acc 97.50

Abbreviations: Acc, accuracy; F1, F1 score; Sen, sensitivity; Spe, specificity.

*Square parentheses indicate the number of rotations for each wavelet in each filter bank.

FIGURE 5 Confusion matrix of cubic support vector machine classifier for the 314 × 481 feature matrix.



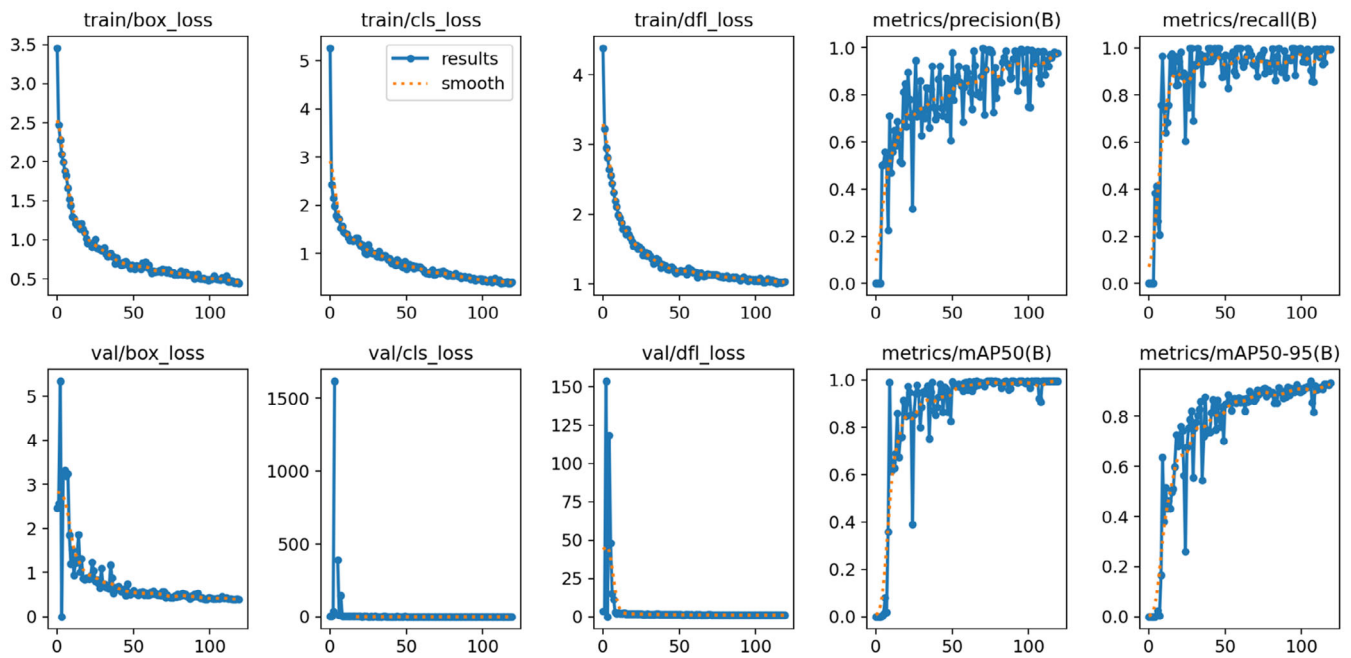


FIGURE 6 Graph plots of the loss function and performance parameters with several training and validation epochs for the YOLOv8l model with Adam optimizer. box_loss, bounding box loss; cls_loss, classification loss, dfl_loss, distribution focal loss; mAP50, mean average precision at intersection over union threshold of 0.5; mAP50-95, mean average precision over intersection over union thresholds from 0.5 to 0.95; train, training phase; val, validation phase.

with Adam versus SGD optimizer led to better performance for most models. Among these, the YOLOv8l model with Adam optimizer attained the highest mean average precision metric, mAP50-95, of 94.1%. For the YOLOv8l model with Adam optimizer, with an increasing number of epochs during both training and validation phases, all loss parameters converged toward their minimum values, and performance metrics toward their maximum values (Figure 6). Figure 7 depicts the identification of normal versus dengue-infected lymphocytes by the YOLOv8l model trained with Adam optimizer on sample PBS images of the validation set.

Performance was further evaluated on the test set through five independent experiments. With Adam optimizer, both YOLOv8s and YOLOv8l models attained identical best results: 99.3% accuracy, 100% recall, 98.6% specificity, and 99.4% F1 score (Table 3), with very low rates of misclassification. Figure 8 depicts the identification of normal versus dengue-infected lymphocytes by the YOLOv8s model trained with Adam optimizer on sample PBS images of the test set.

4 | DISCUSSION

Dengue fever is a viral disease characterized by a wide range of clinical presentations. With the digitization of whole-slide pathological images, the field of digital

pathology has grown apace in recent years. The emergence of machine learning tools promises fully automated diagnostic models that can enable rapid and accurate analysis of images without human intervention. In this study, we focused on two different approaches for diagnosing dengue infection based on the classification of lymphocytes on PBS images. In the first approach, lymphocytes were analyzed using WST, and machine learning classifiers were trained on the extracted wavelet scattering features. Among five tested classifiers, SVM attained the best performance, with 98.70% accuracy, 97.55% sensitivity, 100.00% specificity, and 98.76% F1 score on the robust 10-fold CV. In the second approach involving transfer learning-enabled object detection with YOLOv8 algorithms, the YOLOv8s and YOLOv8l models with Adam optimizer outperformed other variants, attaining identical excellent mean performance results across multiple experiments: $99.3\% \pm 1.4\%$ accuracy, $100.0\% \pm 0.0\%$ recall, $98.6\% \pm 2.9\%$ specificity, and $99.4\% \pm 1.3\%$ F1 score.

The existing literature on automated dengue diagnosis primarily focuses on white blood cell, platelet count, symptoms and biomarker analysis, or their combinations. Tantikitti et al.⁶⁵ used white blood cell count as a differentiation feature to classify dengue viral infections using DT methods. Their model attained only a modest 72.3% accuracy. Hassan et al.⁶⁶ used Raman spectroscopy to detect the dengue virus in human sera. Applying a

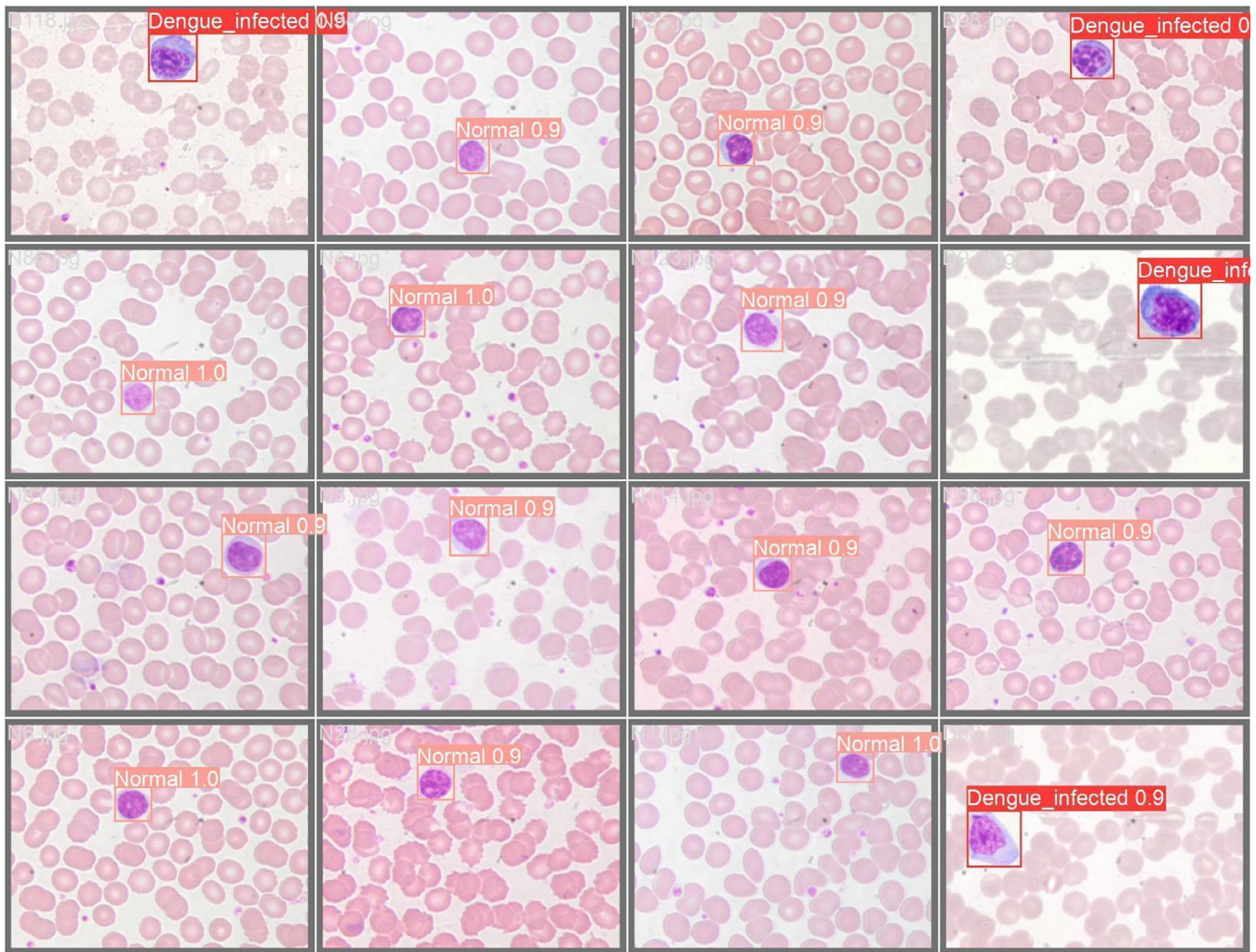


FIGURE 7 Sample peripheral blood smear images of the validation dataset showing normal and dengue-infected lymphocytes identified by the YOLOv8l model with Adam optimizer. The bounding box shows the label and confidence score of the detected object.

TABLE 3 Performance of YOLOv8 variants for dengue detection across five independent experiments on the test dataset stratified by model and optimizer.

Model	Optimizer	Accuracy (%)	Recall (%)	Specificity (%)	F1 score (%)
YOLOv8n	Adam	98.1 ± 1.7	98.1 ± 2.6	98.6 ± 2.9	98.4 ± 1.4
YOLOv8n	SGD	97.5 ± 2.6	97.9 ± 4.7	97.3 ± 3.6	97.7 ± 2.3
YOLOv8s	Adam	99.3 ± 1.4	100.0 ± 0.0	98.6 ± 2.9	99.4 ± 1.3
YOLOv8s	SGD	96.2 ± 2.6	95.1 ± 4.7	98.6 ± 2.9	96.8 ± 2.0
YOLOv8m	Adam	98.7 ± 1.7	98.0 ± 2.6	100.0 ± 0.0	99.0 ± 1.3
YOLOv8m	SGD	96.2 ± 1.4	95.7 ± 4.8	97.1 ± 3.9	96.6 ± 1.6
YOLOv8l	Adam	99.3 ± 1.4	100.0 ± 0.0	98.6 ± 2.9	99.4 ± 1.3
YOLOv8l	SGD	96.8 ± 3.1	96.2 ± 5.2	98.6 ± 2.9	97.4 ± 2.5
YOLOv8x	Adam	98.1 ± 2.7	97.6 ± 5.3	98.6 ± 2.9	98.1 ± 2.7
YOLOv8x	SGD	96.8 ± 5.4	95.7 ± 9.4	98.6 ± 2.9	97.0 ± 5.1

Note: Results are expressed as means ± standard deviations.

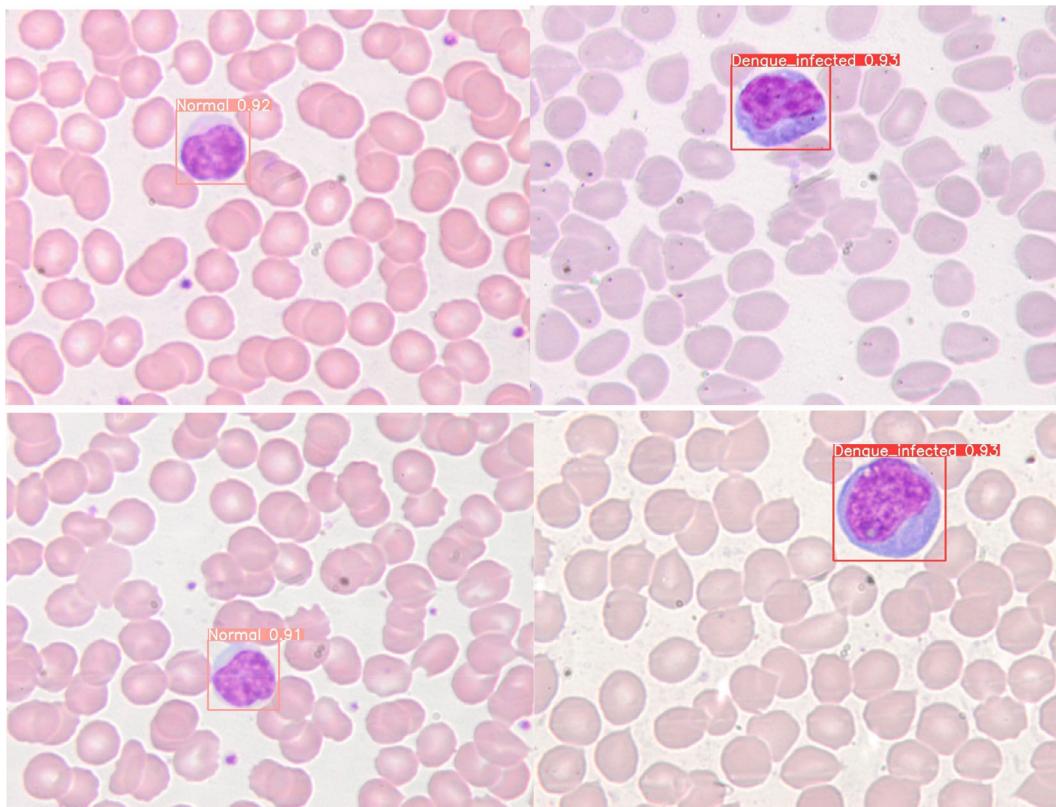


FIGURE 8 Sample peripheral blood smear images of the test set showing normal and dengue-infected lymphocytes identified by the YOLOv8s model with Adam optimizer. The bounding box shows the label and confidence score of the detected object.

pre-trained ResNet101 deep network on Raman spectroscopic data, their transfer learning model attained 96.0% accuracy on test data for dengue infection diagnosis. Mayrose et al.²⁷ studied morphologic characteristics of platelets and lymphocytes on PBS for dengue detection. Using standard shallow SVM and DT classifiers, they attained 93.62% accuracy. Incorporating feature extraction with MobileNetV2 and local binary pattern yielded an accuracy of 95.74% with SVM. Falconi-Agapito et al.⁶⁷ employed a random forest to diagnose dengue infection based on peptide biomarkers. For a targeted specificity >80%, their model attained sensitivities of 72.3% and 88.9%–89.1% for different sample combinations. Hoyos et al.⁶⁸ introduced a clinical decision-support system that utilized a fuzzy cognitive map constructed from signs, symptoms, and routine laboratory tests performed for dengue diagnosis. Their model attained 89.4% accuracy.

To the best of our knowledge, no previous research has explored the use of WST and the YOLOv8 algorithm for diagnosing dengue based on lymphocyte features on PBS. Of note, our model has outperformed the mentioned published models (Table 4). Moreover, machine learning using shallow classifiers has exhibited substantially good results comparable to an object detection network like YOLO. Currently, the models have been trained and

studied with datasets that have an ample quantity of images after the augmentation process. However, we strived to utilize most of the resources available to generate meaningful insights to the best of our abilities. Importantly, our PBS-based strategy lends itself to high-throughput screening of laboratory digitized PBS readouts for dengue detection in hospital and clinic settings.

In addition to the application of YOLO to PBS images for object detection, this algorithm can be leveraged for WSI scans. With regard to YOLO's remarkable ability for multiple object detection, it can effectively identify regions of interest in WSIs and thus aid in the automated detection and diagnosis of various pathological conditions. Another potential direction for the future scope of YOLO lies in enabling remote access for pathologists and clinicians by developing applications for Android and iOS devices. This would give them the flexibility to perform real-time diagnostics regardless of their location. Additionally, other features could be incorporated to further enhance the accessibility and collaborative potential of the YOLO algorithm. Furthermore, the performance of both YOLO algorithms and WST can be assessed by applying them to different datasets across diverse scenarios and evaluating their applicability in clinical settings. This would provide insights into the

TABLE 4 Comparison of the literature with our proposed methods for automated dengue detection.

Authors	Methods	Model input	Best results (%)
Tantikitti et al. (2015) ⁶⁵	White blood cell count-based detection using decision tree	264 peripheral blood smear images	Accuracy 72.3 Sensitivity 71.2 Specificity 73.3
Hassan et al. (2021) ⁶⁶	Raman spectroscopy-based classification using ResNet101	2000 Raman spectral images of sera	Accuracy 96.0 Sensitivity 97.3 Specificity 94.5
Mayrose et al. (2022) ²⁷	Morphological and gray-level spatial dependence matrix feature-based classification using support vector machine	94 peripheral blood smear images	Accuracy 95.74 Sensitivity 98.15 Specificity 92.50
Falconi-Agapito et al. (2022) ⁶⁷	Peptide biomarker based-classification using random forest	323 serum samples	Sensitivity 89.1
Hoyos et al. (2022) ⁶⁸	Clinical decision-support systems based on fuzzy cognitive maps	22 variables: symptoms, signs, lab tests	Accuracy 89.4
Our wavelet scattering method	Wavelet scattering transform-based classification using support vector machine	314 peripheral blood smear images	Accuracy 98.70 Sensitivity 97.55 Specificity 100.0
Our object detection method	Object detection using YOLOv8	314 peripheral blood smear images	Accuracy 99.3 Sensitivity 100.0 Specificity 98.6

robustness of these methods and help validate their real-world usability. Certainly, this research has laid the groundwork for the next benchmark in the domain. Efforts can be made to improve the accuracy and speed of detection using these techniques. By reducing computational time, clinicians would be able to analyze pathological images more quickly, leading to faster diagnosis and treatment decisions.

5 | CONCLUSION

Dengue infection is a global health concern, and characteristic morphological changes in lymphocytes can be seen on PBS images in cases of dengue infection. In this study, we employed two computer vision approaches to detect and classify dengue-infected versus normal lymphocytes from a unique dataset of PBS images. In the WST-based machine learning approach, spatial-time wavelet scattering features were used as input for shallow classifiers. The SVM classifier achieved an excellent 98.70% accuracy. In the object detection approach using the latest version of YOLO, YOLOv8s and YOLOv8l models demonstrated excellent mean classification accuracy of $99.3\% \pm 1.4\%$ across five independent experiments. Furthermore, we have also demonstrated the feasibility of training both models on a relatively small prospective 314-image PBS image dataset. In future works, we will extend the use of WST- and YOLOv8-based computer vision methods with

ablation studies to other applications in the field of digital pathology. This could include diverse clinical diagnostic problems and image datasets and evaluate their efficacy in various real-world clinical settings.

AUTHOR CONTRIBUTIONS

Liora Rosvin Dsilva: Software, Data curation, writing original Draft; Shivani Harish Tantri: Software, Visualization; Niranjana Sampathila: Conceptualization, methodology, Supervision; Hilda Mayrose: Formal analysis, resource; G. Muralidhar Bairy: Methodology, Writing – review and editing; Sushma Belurkar: Validation, Data curation; Kavitha Saravu: Validation, visualization; Krishnaraj Chadaga: writing – review and editing, resources, Abdul Hafeez-Baig: Writing – review and editing, validation.

ACKNOWLEDGMENTS

We would like to thank the Department of Pathology at Kasturba Hospital, MAHE, Manipal, for providing invaluable support in providing the peripheral blood smear slides and the digital microscope set up to capture the peripheral blood smear images required for this work. Furthermore, we would also like to thank the Department of Immunohaematology, Kasturba Hospital, MAHE, Manipal, for providing blood samples from healthy blood bank donors.

CONFLICT OF INTEREST STATEMENT

The authors declare no conflicts of interest.

DATA AVAILABILITY STATEMENT

The data that support the findings of this study are available on request from the corresponding author. The data are not publicly available due to privacy or ethical restrictions.

ORCID

Niranjana Sampathila  <https://orcid.org/0000-0002-3345-360X>

REFERENCES

- Burden of mosquito-borne diseases Parasites & Vectors Open Access across rural versus urban areas in Cameroon between 2002 and 2021: prospective for community-oriented vector management Approaches.
- Ligsay A, Telle O, Paul R. Challenges to mitigating the urban health burden of mosquito-borne diseases in the face of climate change. *Int J Environ Res Public Health*. 2021;18(9):5035.
- Kraemer MU, Reiner RC Jr, Brady OJ, et al. Past and future spread of the arbovirus vectors *Aedes aegypti* and *Aedes albopictus*. *Nat Microbiol*. 2019;4(5):854-863.
- Murray NEA, Quam MB, Wilder-Smith A. Epidemiology of dengue: past, present and future prospects. *Clin Epidemiol*. 2013;5:299-309.
- Jing Q, Wang M. Dengue epidemiology. *Glob Health J*. 2019;3(2):37-45.
- WHO. WHO | Dengue and Severe Dengue. WHO international media factsheet; 2012.
- Khetarpal N, Khanna I. Dengue fever: causes, complications, and vaccine strategies. *J Immunol Res*. 2016;2016:6803098.
- Roy MG, Islam MM, Singh A. Prevalence of dengue virus, their infection, diagnosis, and challenges. *J Appl Biol Biotechnol*. 2023;11(3):20-27.
- Kok BH, Lim HT, Lim CP, Lai NS, Leow CY, Leow CH. Dengue virus infection—a review of pathogenesis, vaccines, diagnosis and therapy. *Virus Res*. 2022;324:199018.
- Kabir MA, Zilouchian H, Younas MA, Asghar W. Dengue detection: advances in diagnostic tools from conventional technology to point of care. *Biosensors*. 2021;11(7):206.
- Parkash O, Hanim Shueb R. Diagnosis of dengue infection using conventional and biosensor based techniques. *Viruses*. 2015;7(10):5410-5427.
- Bera K, Schalper KA, Rimm DL, Velcheti V, Madabhushi A. Artificial intelligence in digital pathology—new tools for diagnosis and precision oncology. *Nat Rev Clin Oncol*. 2019;16(11):703-715.
- Tizhoosh HR, Pantanowitz L. Artificial intelligence and digital pathology: challenges and opportunities. *J Pathol Informat*. 2018;9(1):38.
- Brixtel R, Bougleux S, Lézoray O, et al. Whole slide image quality in digital pathology: review and perspectives. 2022 IEEE access, whole slide image quality in digital pathology: review and perspectives.
- da Silva Neto SR, Tabosa Oliveira T, Teixeira IV, et al. Machine learning and deep learning techniques to support clinical diagnosis of arboviral diseases: a systematic review. *PLoS Negl Trop Dis*. 2022;16(1):e0010061.
- Walter W, Pohlkamp C, Meggendorfer M, et al. Artificial intelligence in hematological diagnostics: game changer or gadget? *Blood Rev*. 2022;58:101019.
- Vyshnav MT, Sowmya V, Gopalakrishnan EA, Variyar V.V S, Menon VK, Soman K. *Deep Learning Based Approach for Multiple Myeloma Detection, 2020 11th International Conference on Computing, Communication and Networking Technologies (ICCCNT)*. IEEE 2020;Vol 2020:1-7. doi:10.1109/ICCCNT49239.2020.9225651
- Salvi M, Michielli N, Meiburger K, et al. Cyto-Knet: an instance segmentation approach for multiple myeloma plasma cells using conditional kernels. *Int J Imag Syst Technol*. 2023;4(5):1-8. doi:10.1002/ima.22984
- Salvi M, Acharya UR, Molinari F, Meiburger KM. The impact of pre-and post-image processing techniques on deep learning frameworks: a comprehensive review for digital pathology image analysis. *Comput Biol Med*. 2021;128:104129.
- Esteva A, Chou K, Yeung S, et al. Deep learning-enabled medical computer vision. *NPJ Digital Med*. 2021;4(1):5.
- Pathak AR, Pandey M, Rautaray S. Application of deep learning for object detection. *Proc Comp Sci*. 2018;132:1706-1717.
- Mohammed EA, Mohamed MM, Far BH, Naugler C. Peripheral blood smear image analysis: a comprehensive review. *J Pathol Informat*. 2014;5(1):9.
- Wani SUD, Khan NA, Thakur G, et al. Utilization of artificial intelligence in disease prevention: diagnosis, treatment, and implications for the healthcare workforce. *Healthcare*. Vol 10. MDPI; 2022:608.
- Bohr A, Memarzadeh K. The rise of artificial intelligence in healthcare applications. *Artificial Intelligence in Healthcare*. Academic Press; 2020:25-60.
- Yunus YM, Narowi M, Lai HI. Morphological features analysis in pathogenic dengue infection as an alternative screening method. *Int J Acad Res Bus Soc Sci*. 2017;7:801-811.
- Clarice CSH, Abeyesuriya V, de Mel S, et al. Atypical lymphocyte count correlates with the severity of dengue infection. *PLoS One*. 2019;14(5):e0215061.
- Mayrose H, Bairy GM, Sampathila N, Belurkar S, Saravu K. Machine learning-based detection of dengue from blood smear images utilizing platelet and lymphocyte characteristics. *Diagnostics*. 2023;13(2):220.
- Deb N, Chakraborty S. A noble technique for detecting anemia through classification of red blood cells in blood smear. *International Conference on Recent Advances and Innovations in Engineering (ICRAIE-2014)*. IEEE; 2014:1-9.
- Bashar MK. Improved classification of malaria parasite stages with support vector machine using combined color and texture features. *2019 IEEE Healthcare Innovations and Point of Care Technologies, (HI-POCT)*. IEEE; 2019:135-138.
- Moshavash Z, Danyali H, Helfroush MS. An automatic and robust decision support system for accurate acute leukemia diagnosis from blood microscopic images. *J Digit Imaging*. 2018;31:702-717.
- Nikitaev VG, Nagornov OV, Pronichev AN, Polyakov EV, Dmitrieva VV. The blood smear image processing for the acute leukemia diagnostics. *Inter J Bio Biomed Eng*. 2016;10:109-114.
- Mayrose H, Sampathila N, Bairy GM, et al. Intelligent algorithm for detection of dengue using mobilenetv2-based deep

- features with lymphocyte nucleus. *Expert Syst.* 2023;40(4):e12904.
33. Nawa K, Suryani E, Prasetyo H. Dengue virus infected leukocyte classification on microscopic images with image histogram based support vector machine. *2019 5th International Conference on Science and Technology (ICST)*. Vol 1. IEEE; 2019:1-5.
 34. Bruna J, Mallat S. Invariant scattering convolution networks. *IEEE Trans Pattern Anal Mach Intell.* 2013;35(8):1872-1886.
 35. Andén J, Mallat S. Deep scattering spectrum. *IEEE Transact Signal Process.* 2014;62(16):4114-4128.
 36. Mallat S. Group invariant scattering. *Commun Pure Appl Mathemat.* 2012;65(10):1331-1398.
 37. Sifre L, Mallat S. Rotation, scaling and deformation invariant scattering for texture discrimination. 2013 IEEE conference on computer vision and pattern recognition. pp. 1233-1240 2013. doi:10.1109/CVPR.2013.163
 38. Aryanmehr S, Boroujeni FZ. Efficient deep CNN-based gender classification using iris wavelet scattering. *Multimed Tools Appl.* 2023;82(12):19041-19065.
 39. Agboola HA, Zaccheus JE. Wavelet image scattering based glaucoma detection. *BMC Biomed Eng.* 2023;5(1):1.
 40. Razali NF, Isa IS, Sulaiman SN, Karim NKA, Osman MK. CNN-wavelet scattering textural feature fusion for classifying breast tissue in mammograms. *Biomed Signal Process Control.* 2023;83:104683.
 41. <https://docs.ultralytics.com/>
 42. Rocha M, Claro M, Neto L, Aires K, Machado V, Veras R. Malaria parasites detection and identification using object detectors based on deep neural networks: a wide comparative analysis. *Comp Methods Biomech Biomed Eng: Imag Visual.* 2022;11:351-368.
 43. Jia D, He Z, Zhang C, Yin W, Wu N, Li Z. Detection of cervical cancer cells in complex situation based on improved YOLOv3 network. *Multimed Tools Appl.* 2022;81(6):8939-8961.
 44. Khandekar R, Shastry P, Jaishankar S, Faust O, Sampathila N. Automated blast cell detection for acute lymphoblastic leukemia diagnosis. *Biomed Signal Process Control.* 2021;68:102690.
 45. <https://www.mathworks.com/help/wavelet/ug/digit-classification-with-wavelet-scattering.html>
 46. <https://www.mathworks.com/help/wavelet/ug/texture-classification-with-wavelet-image-scattering.html>
 47. <https://www.mathworks.com/help/wavelet/ug/wavelet-scattering.html>
 48. Toma RN, Gao Y, Piltan F, et al. Classification framework of the bearing faults of an induction motor using wavelet scattering transform-based features. *Sensors.* 2022;22(22):8958.
 49. Ahmad MZ, Kamboh AM, Saleem S, Khan AA. Mallat's scattering transform based anomaly sensing for detection of seizures in scalp EEG. *IEEE Access.* 2017;5:16919-16929.
 50. Rajendra Acharya U, Vinitha Sree S, Muthu Rama Krishnan M, Molinari F, Garberoglio R, Suri JS. Non-invasive automated 3D thyroid lesion classification in ultrasound: a class of ThyroScanTM systems. *Ultrasonics.* 2012;52(4):508-520. doi:10.1016/j.ultras.2011.11.003
 51. Ren G, Wang Y, Ning J, Zhang Z. Using near-infrared hyperspectral imaging with multiple decision tree methods to delineate black tea quality. *Spectrochim Acta A Mol Biomol Spectrosc.* 2020;237:118407.
 52. Huberty CJ. Discriminant analysis. *Rev Educ Res.* 1975;45(4):543-598.
 53. Ali MZ, Shabbir MNSK, Liang X, Zhang Y, Hu T. Machine learning-based fault diagnosis for single-and multi-faults in induction motors using measured stator currents and vibration signals. *IEEE Transact Industry App.* 2019;55(3):2378-2391.
 54. Cortes C, Vapnik V. Support-vector networks. *Mach Learn.* 1995;20(3):273-297. doi:10.1023/A:1022627411411
 55. Mar T, Zaunseder S, Martínez JP, Llamedo M, Poll R. Optimization of ECG classification by means of feature selection. *IEEE Transact Biomed Eng.* 2011;58(8):2168-2177.
 56. Verma GK, Tiwary US. Multimodal fusion framework: a multi-resolution approach for emotion classification and recognition from physiological signals. *Neuroimage.* 2014;102:162-172.
 57. Tien Bui D, Tuan TA, Klempe H, Pradhan B, Revhaug I. Spatial prediction models for shallow landslide hazards: a comparative assessment of the efficacy of support vector machines, artificial neural networks, kernel logistic regression, and logistic model tree. *Landslides.* 2016;13:361-378.
 58. <https://ultralytics.com/yolov5>
 59. Lou H, Duan X, Guo J, et al. DC-YOLOv8: small-size object detection algorithm based on camera sensor. *Electronics.* 2023; 12(10):2323.
 60. Terven J, Cordova-Esparza D. A comprehensive review of YOLO: from YOLOv1 to YOLOv8 and beyond. *arXiv.* 2023; preprint arXiv:2304.00501.
 61. Ju RY, Cai W. Fracture detection in pediatric wrist trauma X-ray images using YOLOv8 algorithm. *arXiv.* 2023; preprint arXiv:2304.05071.
 62. <https://github.com/ultralytics/ultralytics/issues/189>
 63. https://alumentations.ai/docs/api_reference/augmentations/blur/transforms/
 64. https://alumentations.ai/docs/api_reference/augmentations/transforms/
 65. Tantikitti S, Tumswadi S, Premchaiswadi W. Image processing for detection of dengue virus based on WBC classification and decision tree. *2015 13th International Conference on ICT and Knowledge Engineering (ICT & Knowledge Engineering 2015)*. IEEE; 2015:84-89.
 66. Hassan M, Ali S, Saleem M, et al. Diagnosis of dengue virus infection using spectroscopic images and deep learning. *PeerJ Comp Sci.* 2022;8:e985.
 67. Falconi-Agapito F, Kerkhof K, Merino X, et al. Peptide biomarkers for the diagnosis of dengue infection. *Front Immunol.* 2022;13:793882.
 68. Hoyos W, Aguilar J, Toro M. A clinical decision-support system for dengue based on fuzzy cognitive maps. *Health Care Manag Sci.* 2022;25:666-681.

How to cite this article: Dsilva LR, Tantri SH, Sampathila N, et al. Wavelet scattering- and object detection-based computer vision for identifying dengue from peripheral blood microscopy. *Int J Imaging Syst Technol.* 2024;34(1):e23020. doi:10.1002/ima.23020